Ultrasound Imaging Enables Longitudinal Tracking of Vascular Changes that Correlate with Immune Response After Radiotherapy

Shannon E. Martello[1], Jixin Xia[2], Jiro Kusunose[3], Benjamin C. Hacker[1], McKenzie A. Mayeaux[2], Erica J. Lin[4], Adrienne Hawkes[3], Aparna Singh[3], Charles F. Caskey[3], Marjan Rafat[1,2,5]*

[1]Department of Chemical and Biomolecular Engineering, Vanderbilt University, Nashville, TN, USA

[2] Department of Biomedical Engineering, Vanderbilt University, Nashville, TN, USA

[3] Department of Radiology, Vanderbilt University Medical Center, Nashville, TN, USA

[4] Department of Biological Sciences, Vanderbilt University, Nashville, TN, USA

[5]Department of Radiation Oncology, Vanderbilt University Medical Center, Nashville, TN, USA

*Author for correspondence: Marjan Rafat, PhD, Engineering and Science Building, Rm. 426, Vanderbilt University, Nashville, TN 37212. Phone: (615) 343-3389, Fax: (615) 343-7951, E-mail: marjan.rafat@vanderbilt.edu

Abstract

Background: While immunotherapy shows great promise in patients with triple negative breast cancer, many will not respond to treatment. Radiotherapy has the potential to prime the tumor-immune microenvironment for immunotherapy. However, predicting response is difficult due to tumor heterogeneity across patients, which necessitates personalized medicine strategies that incorporate tumor tracking into the therapeutic approach. Here, we investigated the use of ultrasound (US) imaging of the tumor vasculature to monitor the tumor response to treatment.

Methods: We utilized ultrafast power doppler US to longitudinally track the vascular response to radiotherapy. We used 4T1 (metastatic) and 67NR (non-metastatic) breast cancer models to determine if US measurements corroborate conventional histological analysis of tumor vessels. To evaluate the effects of radiation, tumor volume and vascular index were calculated using US, and the correlation between vascular changes and immune cell infiltration was determined.

Results: US tumor measurements and the quantified vascular response to radiation were confirmed with caliper measurements and immunohistochemistry staining, respectively, demonstrating a proof-of-principle method for non-invasive vascular monitoring. Additionally, we found significant infiltration of $CD8^+$ T cells into irradiated tumors 10 days after radiation, which followed a sustained decline in vascular index and an increase in splenic $CD8^+$ T cells that was first observed 1 day post-radiation.

Conclusions: Our findings reveal that ultrafast power doppler US can evaluate changes in tumor vasculature that are indicative of shifts in the tumor-immune microenvironment. This work may lead to improved patient outcomes through observing and predicting response to therapy.

Keywords:

Ultrasound; Radiotherapy; vasculature; triple negative breast cancer; immune response; immunotherapy

Introduction

The incidence of breast cancer is rising, with over 300,000 new diagnoses annually [1]. Approximately 15% of cases are identified as triple negative breast cancer (TNBC), which is characterized by a disproportionally high death rate due to its aggressive nature and lack of targeted therapies [2,3]. Radiotherapy (RT) is a mainstay of TNBC treatment and significantly reduces the risk of recurrence after surgery [4–6]. RT exerts biological effects beyond tumor cell killing on both short- and long-term scales, altering physical and molecular vascular characteristics and influencing immune cell infiltration and phenotype [7–9]. Recently, it has been suggested that RT can be used as a tool to elicit immune cell infiltration and activation in the tumor, thereby improving the efficacy of immunotherapies in otherwise immunologically "cold" tumors [10–12]. While some TNBC patients respond well to immunotherapies like immune-checkpoint blockade [13–15], it remains difficult to predict therapeutic outcomes due to varying degrees of malignancy, immune landscape, and tumor heterogeneity across patients.

The tumor vasculature influences the therapeutic response molecularly and physically by controlling immune cell trafficking, anti-tumor immunity, and drug delivery. Changes in microvascular structure are indicative of tumor progression and have been implicated in predicting response to RT [16–18]. Recent work has also linked vascular changes in skin cancer with immune cell infiltrates and response to immunotherapy, demonstrating a critical connection between tumor vasculature and the immune system [19]. Non-invasive monitoring of the tumor vasculature post-RT could therefore be used to predict response to immunotherapy.

Previous studies used contrast-enhanced ultrasound (US) to differentiate vessel sizes and measure fibrosarcoma response to radiation [18,20] and high frequency power doppler US to monitor breast tumor response to RT and anti-angiogenic therapy [21]. Here, we use ultrafast power doppler US to measure longitudinal changes in tumor vasculature. Ultrafast US combines improved resolution and sensitivity, allowing for deeper penetration of tissues and more

accurate reconstruction of vascular changes over time [22,23]. In this study, ultrafast US images were taken at multiple timepoints following tumor irradiation in two TNBC models with varying metastatic capacity to investigate vascular dynamics and immune cell infiltration after RT. We found that vascular responses to RT determined by US imaging correspond with histological staining as well as local and systemic immune responses, demonstrating the potential of ultrafast power doppler US to non-invasively track the vasculature after therapy and predict shifts in the immune microenvironment.

Methods

Radiation

Animal studies were performed in accordance with the institutional guidelines and protocols approved by the Vanderbilt University Institutional Animal Care and Use Committee. Female BALB/c mice (8-10 weeks old) were inoculated with $5x10^4$ 4T1 or $1x10^6$ 67NR murine TNBC cells. Tumor length and width were measured using digital calipers (Fisher Scientific) beginning one (4T1) or two (67NR) weeks post-inoculation. Tumor volume was estimated by volume = $(L_1^2xL_2)/2$, where L_1 is the smallest and L_2 is the largest measurement of the tumor. At 100 mm^3, tumors were irradiated to 12 Gy using a 300 kVp cabinet x-ray system filtered with 1.57 mm Al. Mice were anesthetized with 2.5% isoflurane and shielded using a 2 cm thick Cerrobend shield with 1 cm wide and 1.5 cm long apertures to expose the tumors. Transmission through the shield was less than 1%.

US Imaging Protocol

Animals were anesthetized with 1.5-2% isoflurane. An imaging array (L12-5, Philips, Reedsville, PA) was acoustically coupled to the palpable tumor target through a 6 cm tall cavity filled with warm degassed water. A Verasonics Vantage Ultrasound system (Verasonics Inc, Kirkland, WA, USA) was used for imaging planning and acquisition. Real-time B-mode and power doppler imaging were used to check coupling quality, locate tumor center, and identify the spatial extent

of the tumor in the elevational direction. Microbubbles were made in-house using established techniques and administered via retro-orbital injection. To capture a volumetric image of the tumor, 6-12 image planes were acquired with 1-mm spacing to capture [24]. For each plane, 5100 frames of radio frequency (RF) data were acquired at frame rate of 510 Hz at 8.9 MHz. Each frame was comprised of 3 angled compounding planes ranging from -18° to 18°. The acquired RF data was reconstructed offline to in-phase and quadrature (IQ) data.

US offline processing

Motion correction was performed every 30 frames. The mean of each frame was taken and normalized by the 30 frame median. The standard deviation of 15 frames with low mean amplitude was used to calculate a stability threshold. Outlier frames that exceeded the threshold were replaced with linear interpolation from the remaining frames [25]. The motion corrected IQ data was then passed through a singular value decomposition (SVD) filter with 5% cutoff, a Butterworth bandpass filter from 25 Hz to 125 Hz, and a Top-hat filter with 2 mm disk size to help remove static tissue signal and enhance moving signals that depicts vasculature. The filtered data was then summed to produce a power doppler image. The summed power doppler images were passed through Frangi filter that enhanced tubular structures [26]. The tumor region was manually segmented from power doppler images overlayed on the corresponding B-mode images using MATLAB ginput function (The MathWorks, Inc., Natick, Massachusetts, US). Total tumor volume was evaluated by summing the volume for each acquired plane. The dimmest vessel region on the Frangi filtered image was selected manually with MATLAB ginput and a brightness threshold was calculated by taking the mean of the selected region. A binary mask was generated using the brightness threshold, segmenting the vasculature within the tumor. The total vasculature volume was calculated from the number of voxels in the masks across the planes. The vascular index was determined by calculating the ratio of the total vasculature volume to the total tumor volume.

Histological analysis

At 1 or 10 days post-RT, tumors and spleens (10 days only) were resected and placed in 10% neutral buffered formalin (NBF) for 24h at 4ºC and then in 70% ethanol until embedding in paraffin. Sections (4 µm) were deparaffinized, rehydrated, and boiled in citric acid (10 mM pH 6) for antigen retrieval. For immunofluorescence detection, blocking in 10% donkey serum was followed by overnight incubation at 4ºC with anti-CD31 (1:100; R&D Systems) and subsequent incubation with a donkey anti-goat AlexFluor594 secondary antibody (1:500; Invitrogen). An autofluorescence quenching solution (Vector Laboratories) was used before nuclear staining with 4',6-diamidino-2-phenylindole dihydrochloride (DAPI). For chromogenic detection, sections were treated with 3% hydrogen peroxide and blocking was performed with 10% goat serum, followed by overnight incubation with CD4 or CD8 (Invitrogen, 1:100) primary antibodies. Sections were then sequentially incubated with biotinylated secondary antibodies, substrate from a DAB peroxidase substrate kit (Vector Laboratories), and counterstained with hematoxylin. A no primary control was performed for all conditions in both fluorescence and chromogenic detection to confirm antibody specificity. All samples were imaged using an inverted Leica microscope (DMi8). Fiji was used to quantify percent area of positive CD31 staining and counts of $CD4^+$ and $CD8^+$ cells [27].

Flow Cytometry

At 1 or 10 days post-RT, tumors, spleens, and lungs were resected and minced in serum-free RPMI media. Tumors and lungs were then placed in a 400 µg/mL DNase I and 20 µg/mL Liberase digestion solution and incubated for 30 minutes in a 37ºC water bath. Digestion was stopped by adding RPMI supplemented with 10% fetal bovine serum. Lungs and spleens were then incubated in ACK lysis buffer for 2 minutes before adding 3% FBS in PBS to halt lysis. All cells were stained with Aqua fixable viability stain (ThermoFisher) and FC receptors were blocked with CD16/32 (Biolegend) while simultaneously staining for all surface markers. Cells

were incubated for 20 minutes at 4ºC, rinsed with PBS, and fixed with 1% NBF for at least 20 minutes at 4ºC. Flow cytometry was performed on a four-laser Amnis CellStream machine (Luminex) and FlowJo software (Becton Dickinson) was used for analysis. The following antibody clones were used for analysis: CD45 (30-F11), CD11b (M1/70), F4/80 (BM8), Ly6G (1A8), GR-1 (RB6-8C5), MHCII (M5/114.15.2), CD11c (N418), CD3 (17A2), CD4 (GK1.5), and CD8 (53-6.7).

Statistical Analysis

To determine statistical significance, differences in CD31, CD8, and CD4 expression and in immune cell populations after radiation and between the two tumor types or between timepoints were determined by two-way ANOVA. Student's t-tests were used to determine statistical significance of vascular index between timepoints for each condition and between conditions at each timepoint. Pearson's correlation coefficients were used to determine correlation between tumor volumes derived from ultrasound versus caliper measurements. All statistical analyses were performed in GraphPad Prism 10.

Results

US tracks differences in tumor volume and vascularity over time

To evaluate whether ultrafast US can non-invasively monitor tumor response to RT, metastatic 4T1 and non-metastatic 67NR tumors were irradiated to 12 Gy—a non-curative dose that allowed for the study of both vascular and immune cell changes over time. At 1 day prior to and 1 and 8 days after RT, tumor volume was quantified using B-mode US, and vascularity was quantified using high frame rate doppler US to determine the feasibility of visualizing changes on both short and long timescales (**Figure 1A**). US-derived tumor volumes were overall highly correlated with manual caliper measurements at each timepoint for 67NR (0 Gy) and 4T1 (0,12 Gy) (**Supplemental Figure S1**). Furthermore, linear regression analysis of each radiation condition demonstrated overlapping 95% confidence intervals of slopes and intercepts

(**Supplemental Table S1**), highlighting the ability of US to track with caliper measurements regardless of tumor type and treatment. While the volumes were weakly correlated in irradiated 67NR tumors, US measurements captured the marked stall in 67NR tumor growth after radiation that tracked with caliper measurements (**Figure 1B**), which may be critical to patient care and prediction of therapy response. The differences in calculated volumes in the irradiated 67NR tumors are likely due to the large reduction in tumor volume 8d post-RT that led to errors in caliper measurements due to difficulties in distinguishing the tumor, further highlighting the need for an improved method to track tumor response during treatment. In contrast to the change in growth of 67NR tumors post-RT, the highly metastatic 4T1 tumors were unaffected. Accuracy of the US volume measurements compared to caliper measurements and the ability to detect major changes in tumor volume post-RT reveals the potential of this technique to provide a more quantitative method for tracking growth changes over time post-RT.

Noticeable differences in vascularity between the tumor types and after RT were also observed in US analysis. The vascular index of each tumor was derived from Frangi filtered images and normalized to the measured tumor volume, enabling non-invasive quantification of vascular changes that are independent of tumor size. US images showed that the 67NR tumors were highly vascular (**Figure 2A**). Conversely, 4T1 tumors appeared largely avascular throughout the center, and visualization of vascular networks was difficult, indicating a necrotic core. At 1 day post-RT, 67NR tumors showed a significant decrease in vascular index from 0.17 ± 0.04 to 0.13 ± 0.04 that did not recover up to 1 week later (**Figure 2B**). Control mice bearing 67NR tumors showed a 35% increase from 0.17 ± 0.08 to 0.23 ± 0.17 at 8 days post-RT. There were no significant changes in vascular index in the 4T1 tumors in both irradiated and control mice (**Figure 2C**), and 4T1 tumors exhibited a lower vascular index compared to 67NR at all time points.

Image-derived vascular index correlates with histological analysis

Immunofluorescence staining for CD31 was performed on control and irradiated 67NR and 4T1 tumors to validate and compare the US findings to standard practices of quantifying vascular changes in both pre-clinical and clinical studies. 67NR tumors were characterized by higher vessel density compared to 4T1 tumors in both control and irradiated conditions (**Figure 3A, B**). 4T1 tumors showed no significant changes in vessel density over time or after radiation. Irradiated 67NR tumors exhibited a decrease in vessel density compared to control tumors as soon as 1 day post-RT, which persisted after 10 days, at which point the vessel density was nearly half of the control tumors (**Figure 3C**). Despite the decrease in density, the cross sectional vessel area in irradiated 67NR tumors increased from 1 to 10 days, suggesting radiation-induced vascular remodeling over this timescale (**Figure 3D**). The average vessel size in 4T1 tumors was higher than 67NR vessels across all conditions but showed no significant differences over time or after irradiation. These observations corroborate the trends observed using US imaging, underscoring the feasibility of using US to identify and monitor vascular changes non-invasively over time.

Radiotherapy elicits a local increase in $CD8^+$:$CD4^+$ T cell ratios that follows vascular changes

We next sought to determine whether our non-curative dose of RT produced an immune response that correlated with the vascular changes observed during US imaging. Flow cytometry analysis of tumor-infiltrating myeloid and lymphocyte populations was performed at 1 and 10 days post-RT to identify early and intermediate responses in the local microenvironment. In both 67NR and 4T1 tumors, we did not see any significant changes in immune cells at 1 day post-RT. However, both tumor types showed significantly higher infiltration of $CD45^+$ immune cells at 10 days post-RT (**Figure 4A**). Both irradiated and unirradiated 4T1 tumors showed an increase in immune cells—likely due to tumor growth and increased inflammation—while 67NR tumors showed a significant increase only in irradiated tumors, demonstrating the immune-stimulating effect from a single 12 Gy dose. While tumors showed no changes in the percentage

of $CD11b^+$ myeloid cells over time or between control and irradiated groups, the immune cells in 4T1 tumors were predominantly of myeloid lineage while 67NR tumors were comprised of approximately 50% myeloid cells (**Figure 4B**). No changes in macrophages, dendritic cells (DCs), and neutrophils in either tumor type over time or post-RT were observed (**Supplemental Figure S2**). Both 67NR and 4T1 tumors showed an increase in myeloid-derived suppressor cells (MDSCs) from 1 to 10 days post-RT. However, this increase was abated by RT in 67NR tumors even after 10 days. 4T1 tumors also showed an increase in antigen presenting cells (APCs) over time, though to a lesser extent in irradiated tumors.

An increase in $CD3^+$ T cells in both irradiated and control 67NR tumors from 1 to 10 days post-RT suggests that the overall increase in immune cell populations after 10 days was driven by this population (**Figure 4C**). In 4T1 tumors, we observed no significant changes in total T cells over time or after radiation. Analysis of T cell subpopulations showed increased $CD4^+$ T cell infiltration at 1 day post-RT in 67NR tumors that shifted to an increase in $CD8^+$ T cell infiltration and $CD8^+$:$CD4^+$ T cell ratio at 10d post-RT, which was not observed in 4T1 tumors (**Figure 4D-H**). This highlights the immunostimulatory nature of our radiation scheme and differences in the expected immune landscapes between 67NR and 4T1 tumors. We validated these results using immunohistochemistry staining for CD8 in 67NR tumors, further confirming the ability of radiation to increase cytotoxic T cell infiltration 10 days post-RT (**Figure 4I-L**). In addition, the changes in immune and $CD8^+$ T cell infiltration of irradiated 67NR tumors at 10 days post-RT correlated with the observed decrease in vascularity beginning as early as 1 day post-RT, suggesting the utility of non-invasive vascular monitoring with prediction of immune responses to RT.

Systemic cytotoxic T cell response correlates with vascular changes and precedes local response to RT

Finally, we analyzed changes in immune cell populations in the spleen and lungs at 1 and 10 days post-RT to determine how systemic and distant responses to RT differ from the local response. Interestingly, 67NR-bearing mice exhibited a decrease in splenic $CD4^+$ T cells and increase in $CD8^+$ T cells 1 day post-RT, displaying a significant increase in the $CD8^+$:$CD4^+$ ratio at this timepoint (**Figure 5A-D**). These splenic cell populations returned to control proportions by 10d post-RT, suggesting that the observed local shift in T cell populations in tumors at 10d can be detected systemically and in the vascular index 24h after treatment (**Figure 2B**). In mice with 4T1 tumors, though we observed significant increases in splenic $CD4^+$ T cells from 1 to 10 days post-RT, there was a decrease in splenic $CD8^+$ T cells at 1 day post-RT and overall at 10 days post-RT, leading to a lower $CD8^+$:$CD4^+$ ratio at both timepoints in irradiated compared to control tumors (**Figure 5A-E**). Immunohistochemistry staining of spleens from mice with 67NR and 4T1 tumors at 10 days post-RT further corroborates our findings, showing negligible differences between spleens from irradiated and control 67NR-bearing mice but a visible increase in the $CD4^+$ T cell population in spleens from 4T1-bearing mice by 10d post-RT (**Figure 5F, G**). Analysis of myeloid cell subpopulations did not show significant differences in spleens from either 67NR- or 4T1-bearing mice after radiation, though we observed increased proportions of macrophages, dendritic cells, and neutrophils from 1 to 10 days in 4T1-bearing mice (**Supplemental Figure S3**), likely due to splenomegaly.

Analysis of immune cells in the lungs showed no changes after radiation for either tumor model. However, clear differences in the immune cell populations between lungs in mice with 67NR and 4T1 tumors were detected. While the lungs of mice with 67NR tumors showed no significant increases in $CD45^+$ immune cells over time, the lungs of 4T1-bearing mice exhibited significant increases under both control and irradiated conditions (**Figure 5H**). The immune subpopulations present in the lungs appeared to mirror those in the tumor microenvironment, with lungs dominated by $CD11b^+$ myeloid cells in mice with 4T1 tumors and a substantially higher

proportion of $CD3^+$ T cells in mice with 67NR tumors (**Figure 5I, J**). Analysis of myeloid subpopulations in the lungs also show overall higher proportions in mice with 4T1 compared to 67NR tumors, with the largest differences occurring over time rather than after radiation (**Supplemental Figure S4**). Since 4T1 cells readily metastasize to the lungs while 67NR cells are not metastatic [28], these differences in the immune landscape are expected. Taken together, the consistency of the immune landscape between control and irradiated lungs highlight that our radiation scheme does not impact distant sites while local tumor effects of radiation can be observed systemically beginning 1 day after treatment.

Discussion

With the recent progress in the field of immunotherapy, the limited treatment options for TNBC patients may be expanded through personalized medicine approaches that combine prognostic monitoring with treatment. Non-invasive methods of predicting and tracking tumor response to therapy have the potential to greatly improve patient outcomes. The tumor vasculature is particularly important in this regard as it can give insight into the degree of malignancy and predict drug delivery efficacy and immune cell infiltration to the tumor. In this proof-of-principle study, we used ultrafast power doppler US imaging to track longitudinal, RT-induced vascular changes in two breast cancer models that differ in metastatic capacity. First, we showed that ultrafast power doppler US can non-invasively monitor post-RT vascular changes that correspond to histological characteristics. We then identified that the decrease in vascular index observed via US at 1 day post-RT in 67NR mice corresponded to a splenic increase in $CD8^+$:$CD4^+$ ratio at 1 day post-RT and preceded a significant local increase in the $CD8^+$ cytotoxic T cell population that was only observed in irradiated tumors (**Figure 4**). Together, these data establish our US technique as an accurate method to track longitudinal tumor vasculature changes and a proxy for predicting both systemic and local immune response to RT.

Prior work has tracked tumor response to radio- and immunotherapy using high-frequency (>15MHz) power doppler ultrasound, such as Kaffas et al. who identified the same trend of decreased vasculature 1 day after irradiating MDA-MB-231 tumors to 8 and 16 Gy [21]. Similar reductions in vasculature have also been observed using super harmonic imaging methods that transmit with low frequency pulses and receive at super harmonic frequencies, which allows for high resolution visualization of vasculature [18]. Our system was operated at clinical frequency (<15MHz), implemented with a commercial linear array, and only required a small dose of bolus injection of microbubbles. This system achieved *in vivo* imaging with sub-millimeter level resolution laterally and axially sufficient for visualizing and quantifying rodent microvessels over 15 millimeters below the tissue surface [22]. Out-of-plane sampling of the tumor could improve 3D imaging by decreasing the spacing to a step size lower than one half the elevational resolution of the transducer [29] or using rotational compounding could potentially be performed as in Demené et al. [23]. Overall, microvascular imaging with ultrasound is sensitive to changes that occur during response to cancer therapy and could help inform guidance criteria, such as RECIST (Response Evaluation Criteria in Solid Tumors) [30], by providing non-invasive measurements of functional activity that correspond to known biological responses to radio- or immunotherapy.

Previous work has found the vasculature of 67NR tumors to be substantially different from 4T1 tumors [31,32], which was corroborated by our study. The slower growing 67NR tumors form vessels with a thicker endothelium compared to the 4T1 tumors, which are characterized by leaky, tortuous vasculature and significant areas of necrosis. Based on our US and histological data, it is possible that RT caused damage to the mostly intact 67NR vessels as early as 24 hours post-RT, an effect seen after single doses of RT [33,34]. While the overall vessel coverage across 67NR tumors remained low through 10 days post-RT, we observed a shift toward larger vessels throughout the irradiated tumors that were not seen in the control

samples. Additional analyses of US measurements are required to quantify the number of larger vessels in these tumors. However, this initial observation could indicate radiation-induced vascular remodeling and vascular normalization in agreement with previous studies. For example, in a Lewis lung carcinoma model, a single fraction of 12 Gy irradiation reduced the microvascular density of tumors and increased pericyte coverage, leading to increased perfusion of the tumor compared to controls [35].

The ability of non-ablative RT to induce vascular normalization has also been demonstrated in pancreatic cancer, where a radiation-induced reduction in vascularity and increased in vessel maturation led to increased recruitment and infiltration of T lymphocytes [36,37]. We observed a significantly increased $CD8^+$:$CD4^+$ T cell ratio only in the irradiated 67NR tumors, which also exhibited a sustained decrease in vascularity observed with both US and histology. This may be due to radiation-induced vascular remodeling and upregulation of adhesion molecules [38], though additional US and histological analyses are needed to confirm the direct association between immune cell infiltrate and vascular changes in our model. Because 4T1 tumors are immunologically cold and highly aggressive, a higher dose or fractionated regimen of RT may be necessary to elicit vascular changes and impact immune cell infiltration. We also observed a significant increase in the splenic $CD8^+$:$CD4^+$ T cell ratio of mice with 67NR tumors at 1 day post-RT. This observation is indicative of a systemic response elicited by local radiation, thus corroborating previous reports of this phenomena in pre-clinical studies of RT and immunotherapy [39,40]. While the exact link between changes in splenic and tumor immune cell populations has not been defined, the spleen is demonstrated to be a critical site of immune tolerance to induce anti-tumor immunity [41,42]. Our findings in the splenic response to local tumor irradiation therefore illustrate the potential of RT to be combined with immunotherapy and the need for a method to track and predict the success of combination treatments. The observed vascular change in response to RT in 67NR tumors using non-invasive US imaging

could be used to determine immune cell infiltration and response to therapy as we observed substantial vascular changes after 1 day but no immune cell changes until up to 10 days post-RT. A recent study correlated high vascularity with high inflammation in basal cell carcinomas to predict therapeutic outcomes [19], which underscores the feasibility of using the vascular response to predict immune infiltration. CT imaging biomarkers have also been developed to correlate tumor-immune microenvironment changes with response to immune checkpoint blockade [43], further demonstrating the utility of coupling non-invasive tumor monitoring with evaluating the immune response.

Conclusion

Identifying methods that accurately monitor changes in tumor vasculature longitudinally and non-invasively after therapy may be critical not only for assessing response to adjuvant immunotherapy and determining outcomes early in the treatment process but also for guiding clinical treatment strategies. Future experiments will provide more in depth characterization of vascular changes using US and further link the tumor vasculature and changes in tumor-infiltrating immune cell populations. This work demonstrates the potential for using ultrafast US imaging as a personalized medicine technique to evaluate changes in the tumor microenvironment following RT. Monitoring vascular changes to predict therapy response and shifts in the immune landscape of the tumor may improve outcomes for patients with limited treatment options.

Abbreviations

APC: Antigen presenting cell; DAPI: 4’,6-diamidino-2-phenylindole dihydrochloride ; DC: Dendritic cell; Gy: Gray; IQ: in-phase and quadrature; MDSC: myeloid-derived suppresor cell; NBF: Neutral buffered formalin; RECIST: Response Evaluation Criteria in Solid Tumor; RF: Radiofrequency; RT: radiotherapy; SVD: Single value decomposition; TNBC: Triple negative breast cancer; US: Ultrasound

Acknowledgements

The authors thank Dr. Michael Freeman for irradiator use and Dr. Austin Kirschner and the radiation physics staff for constructing the Cerrobend shield. We also thank the Vanderbilt Translational Pathology Shared Resource (TPSR) supported by NCI/NIH Cancer Center Support Grant P30CA068485 for tissue sample preparation. This research was financially supported by the Focused Ultrasound Foundation Cancer Immunotherapy Award and NIH grant R00CA201304.

Contributions

M.R. and C.F.C conceptualized the study and supervised the project. J.K., J.X., A.H., A.S., and C.F.C developed the ultrasound protocol. S.E.M., J.K., J.X., A.H., B.C.H., M.A.M., A.S., and E.J.L. performed experiments. S.E.M. and J.X. performed data analysis and wrote the manuscript. S.E.M., J.X., J.K., C.F.C, and M.R. revised the manuscript.

Competing Interests

The authors declare no conflicts of interest that could have appeared to influence the work reported in this paper.

References

1. Siegel RL, Giaquinto AN, Jemal A. Cancer statistics, 2024. CA Cancer J Clin. 2024; 74: 12–49.
2. Baranova A, Krasnoselskyi M, Starikov V, et al. Triple-negative breast cancer: current treatment strategies and factors of negative prognosis. Vol. 2022, Journal of Medicine and Life. J Med Life; 2022.
3. Zagami P, Carey LA. Triple negative breast cancer: Pitfalls and progress. npj Breast Cancer. 2022; 8: 1–10.
4. Lowery AJ, Kell MR, Glynn RW, Kerin MJ, Sweeney KJ. Locoregional recurrence after breast cancer surgery: A systematic review by receptor phenotype. Vol. 133, Breast Cancer Research and Treatment. Springer; 2012.
5. Dragun AE, Pan J, Rai SN, Kruse B, Jain D. Locoregional recurrence in patients with triple-negative breast cancer: Preliminary results of a single institution study. Am J Clin Oncol Cancer Clin Trials. 2011; 34: 231–7.
6. Afghahi A, Purington N, Han SS, et al. Higher absolute lymphocyte counts predict lower mortality from early-stage triple-negative breast cancer. Clin Cancer Res. 2018; 24: 2851–8.
7. Choi SH, Kim AR, Nam JK, et al. Tumour-vasculature development via endothelial-to-mesenchymal transition after radiotherapy controls CD44v6+ cancer cell and macrophage polarization. Nat Commun. 2018; 9: 1–18.
8. Vanpouille-Box C, Alard A, Aryankalayil MJ, et al. DNA exonuclease Trex1 regulates radiotherapy-induced tumour immunogenicity. Nat Commun. 2017; 8: 15618.
9. Bouchet A, Serduc R, Laissue JA, Djonov V. Effects of microbeam radiation therapy on normal and tumoral blood vessels. Phys Medica. 2015; 31: 634–41.
10. Wang Y, Liu ZG, Yuan H, et al. The reciprocity between radiotherapy and cancer immunotherapy. Clin Cancer Res. 2019; 25: 1709–17.

11. Galluzzi L, Aryankalayil MJ, Coleman CN, Formenti SC. Emerging evidence for adapting radiotherapy to immunotherapy. Nat Rev Clin Oncol. 2023; 20: 543–57.

12. Aguilera TA, Elghonaimy EA, Shehade H, et al. Induced tumor heterogeneity reveals factors informing radiation and immunotherapy combinations. Clin Cancer Res. 2020; 26: 2972–85.

13. Cyprian FS, Akhtar S, Gatalica Z, Vranic S. Targeted immunotherapy with a checkpoint inhibitor in combination with chemotherapy: A new clinical paradigm in the treatment of triple-negative breast cancer. Vol. 19, Bosnian Journal of Basic Medical Sciences. Association of Basic Medical Sciences of Federation of Bosnia and Herzegovina; 2019.

14. Emens LA, Adams S, Barrios CH, et al. First-line atezolizumab plus nab-paclitaxel for unresectable, locally advanced, or metastatic triple-negative breast cancer: IMpassion130 final overall survival analysis. Ann Oncol. 2021; 32: 983–93.

15. Cortes J, Cescon DW, Rugo HS, et al. Pembrolizumab plus chemotherapy versus placebo plus chemotherapy for previously untreated locally recurrent inoperable or metastatic triple-negative breast cancer (KEYNOTE-355): a randomised, placebo-controlled, double-blind, phase 3 clinical trial. Lancet. 2020; 396: 1817–28.

16. Gessner RC, Aylward SR, Dayton PA. Mapping microvasculature with acoustic angiography yields quantifiable differences between healthy and tumor-bearing tissue volumes in a rodent model. Radiology. 2012; 264: 733–40.

17. Ribatti D, Nico B, Ruggieri S, Tamma R, Simone G, Mangia A. Angiogenesis and Antiangiogenesis in Triple-Negative Breast cancer. Transl Oncol. 2016; 9: 453–7.

18. Kasoji SK, Rivera JN, Gessner RC, Chang SX, Dayton PA. Early assessment of tumor response to radiation therapy using high-resolution quantitative microvascular ultrasound imaging. Theranostics. 2018; 8: 156–68.

19. Sahu A, Kose K, Kraehenbuehl L, et al. In vivo tumor immune microenvironment phenotypes correlate with inflammation and vasculature to predict immunotherapy

response. Nat Commun. 2022; 13: 1–19.

20. Butler M, Perperidis A, Zahra JLM, et al. Differentiation of Vascular Characteristics Using Contrast-Enhanced Ultrasound Imaging. Ultrasound Med Biol. 2019; 45: 2444–55.

21. El Kaffas A, Giles A, Czarnota GJ. Dose-dependent response of tumor vasculature to radiation therapy in combination with Sunitinib depicted by three-dimensional high-frequency power Doppler ultrasound. Angiogenesis. 2013; 16: 443–54.

22. Errico C, Pierre J, Pezet S, et al. Ultrafast ultrasound localization microscopy for deep super-resolution vascular imaging. Nature. 2015; 527: 499–502.

23. Demené C, Payen T, Dizeux A, et al. 3-D Longitudinal Imaging of Tumor Angiogenesis in Mice in Vivo Using Ultrafast Doppler Tomography. Ultrasound Med Biol. 2019; 45: 1284–96.

24. Borden MA, Kruse DE, Caskey CF, Zhao S, Dayton PA, Ferrara KW. Influence of lipid shell physicochemical properties on ultrasound-induced microbubble destruction. IEEE Trans Ultrason Ferroelectr Freq Control. 2005; 52: 1992–2002.

25. Mace E, Montaldo G, Osmanski BF, Cohen I, Fink M, Tanter M. Functional ultrasound imaging of the brain: Theory and basic principles. IEEE Trans Ultrason Ferroelectr Freq Control. 2013; 60: 492–506.

26. Kroon D-J. Hessian based Frangi Vesselness filter - File Exchange - MATLAB Central. MATLAB Central File Exchange. MATLAB Central File Exchange; 2023.

27. Schindelin J, Arganda-Carreras I, Frise E, et al. Fiji: An open-source platform for biological-image analysis. Nat Methods. 2012; 9: 676–82.

28. Aslakson CJ, Miller FR. Selective Events in the Metastatic Process Defined by Analysis of the Sequential Dissemination of Subpopulations of a Mouse Mammary Tumor. Cancer Res. 1992; 52: 1399–405.

29. Smith WL, Fenster A. Optimum scan spacing for three-dimensional ultrasound by speckle statistics. Ultrasound Med Biol. 2000; 26: 551–62.

30. Eisenhauer EA, Therasse P, Bogaerts J, et al. New response evaluation criteria in solid tumours: Revised RECIST guideline (version 1.1). Eur J Cancer. 2009; 45: 228–47.

31. Papiernik D, Urbaniak A, Kłopotowska D, et al. Retinol-binding protein 4 accelerates metastatic spread and increases impairment of blood flow in mouse mammary gland tumors. Cancers (Basel). 2020; 12: 623.

32. Gerwing M, Hoffmann E, Kronenberg K, et al. Multiparametric MRI enables for differentiation of different degrees of malignancy in two murine models of breast cancer. Front Oncol. 2022; 12: 1000036.

33. Wong HH, Song CW, Levitt SH. Early changes in the functional vasculature of Walker carcinoma 256 following irradiation. Radiology. 1973; 108: 429–34.

34. Park HJ, Griffin RJ, Hui S, Levitt SH, Song CW. Radiation-induced vascular damage in tumors: Implications of vascular damage in ablative hypofractionated radiotherapy (SBRT and SRS). Vol. 177, Radiation Research. Allen Press; 2012.

35. Lan J, Wan XL, Deng L, et al. Ablative hypofractionated radiotherapy normalizes tumor vasculature in Lewis lung carcinoma mice model. Radiat Res. 2013; 179: 458–64.

36. Ganss R, Ryschich E, Klar E, Arnold B, Hämmerling GJ. Combination of T-cell therapy and trigger of inflammation induces remodeling of the vasculature and tumor eradication. Cancer Res. 2002; 62: 1462–70.

37. Klug F, Prakash H, Huber PE, et al. Low-Dose Irradiation Programs Macrophage Differentiation to an iNOS+/M1 Phenotype that Orchestrates Effective T Cell Immunotherapy. Cancer Cell. 2013; 24: 589–602.

38. Hallahan D, Kuchibhotla J, Wyble C. Cell adhesion molecules mediate radiation-induced leukocyte adhesion to the vascular endothelium. Cancer Res. 1996; 56: 5150–5.

39. Sharabi AB, Nirschl CJ, Kochel CM, et al. Stereotactic radiation therapy augments antigen-specific PD-1-mediated antitumor immune responses via cross-presentation of tumor antigen. Cancer Immunol Res. 2015; 3: 345–55.

40. Demaria S, Golden EB, Formenti SC. Role of local radiation therapy in cancer immunotherapy. Vol. 1, JAMA Oncology. JAMA Oncol; 2015.

41. Ugel S, Peranzoni E, Desantis G, et al. Immune Tolerance to Tumor Antigens Occurs in a Specialized Environment of the Spleen. Cell Rep. 2012; 2: 628–39.

42. Allen BM, Hiam KJ, Burnett CE, et al. Systemic dysfunction and plasticity of the immune macroenvironment in cancer models. Nat Med. 2020; 26: 1125–34.

43. Sun Z, Zhang T, Ahmad MU, et al. Comprehensive assessment of immune context and immunotherapy response via noninvasive imaging in gastric cancer. J Clin Invest. 2024; 134.

Figures

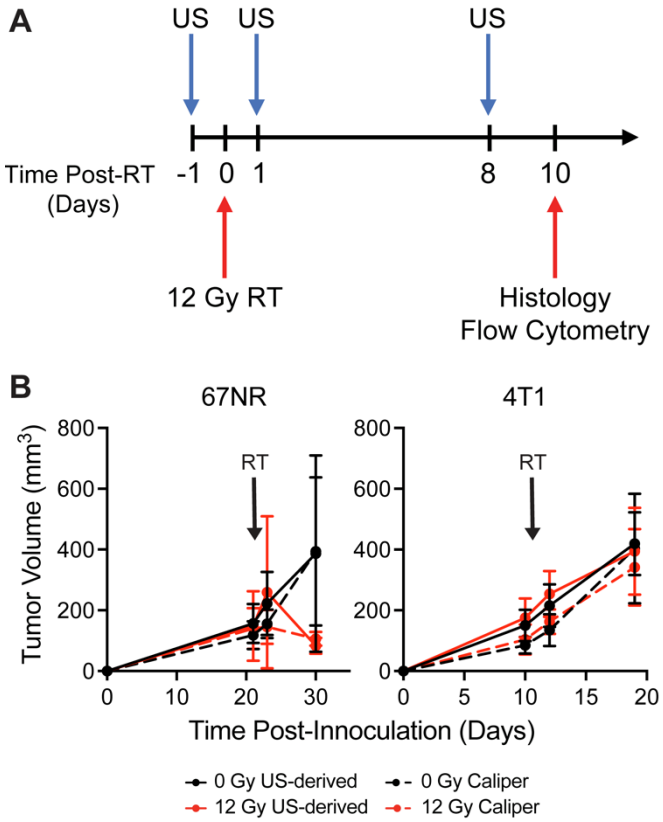

Figure 1. Ultrasound (US) imaging accurately tracks changes in tumor volume post-RT. A. Experimental timeline. 67NR and 4T1 tumors were irradiated to 12 Gy. US imaging was performed 1 day prior to and 1 and 8 days after RT. Tumors were resected at 10 days post-RT for histological and flow cytometric analysis. **B.** Tumor volumes measured via US at -1, 1, and 8 days post-RT (solid lines) compared to manual caliper measurements taken at the same timepoints (dashed lines) for 67NR (n=9 for -1 and 1 day 0 Gy, n=8 for -1 and 1 day 12 Gy, and n=4 for 8 day 0/12 Gy) and 4T1 (n=13 for -1 and 1 day and n=6 for 8 day 0 Gy, n=15 for -1 and 1 day, and n=9 for 8 day 12 Gy) tumors. Error bars show standard deviation.

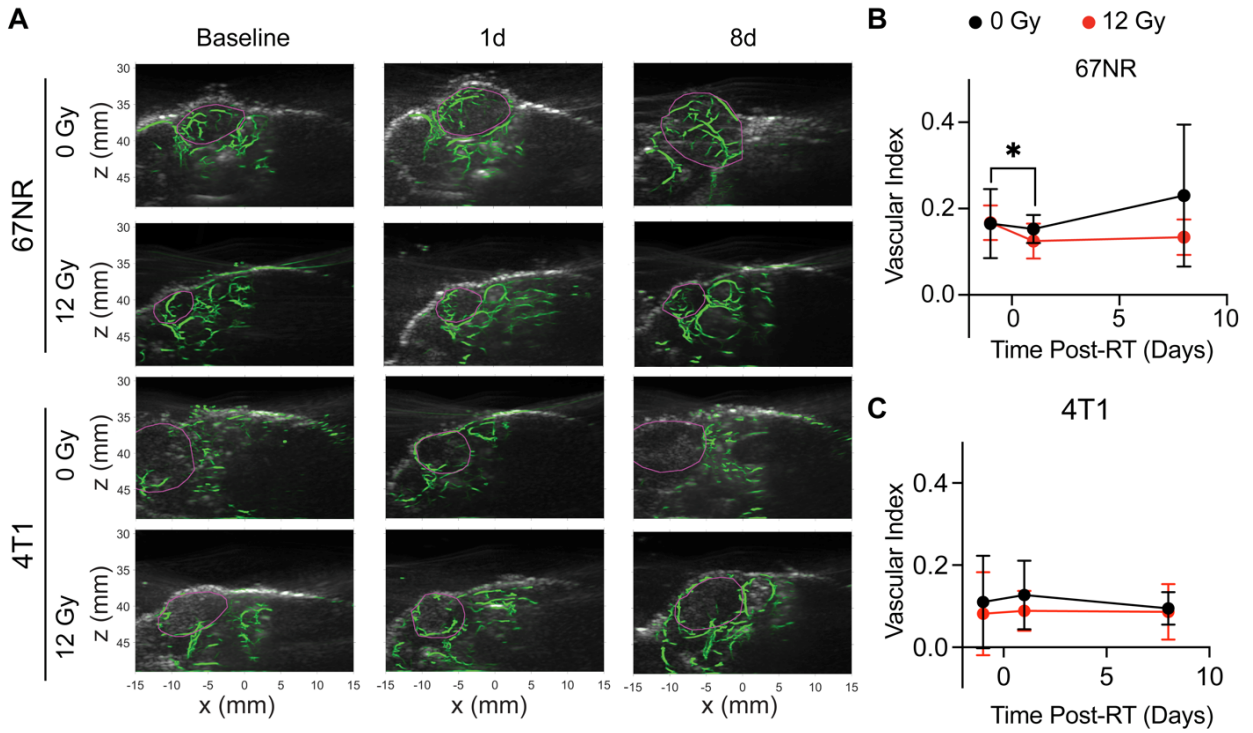

Figure 2. Ultrafast US imaging quantifies vascular changes post-RT. A. Representative images of power doppler images of vascular structure overlaid onto B-mode images of the tumor. Vascular structures imaged with doppler are shown in green. Circles indicate the identified tumor volumes. Quantification of the vascular volume from doppler images and tumor volume from B-mode images enabled calculation of vascular index post-RT over time in **(B)** 67NR (n=9 for -1 and 1 day 0 Gy, n=8 for -1 and 1 day 12 Gy, and n=4 for 8 day 0/12 Gy) and **(C)** 4T1 (n=13 for -1 and 1 day and n=6 for 8 day 0 Gy, n=15 for -1 and 1 day and n=9 for 8 day 12 Gy) tumors. Error bars represent standard deviation with *p<0.05 determined by student's t-test between timepoints.

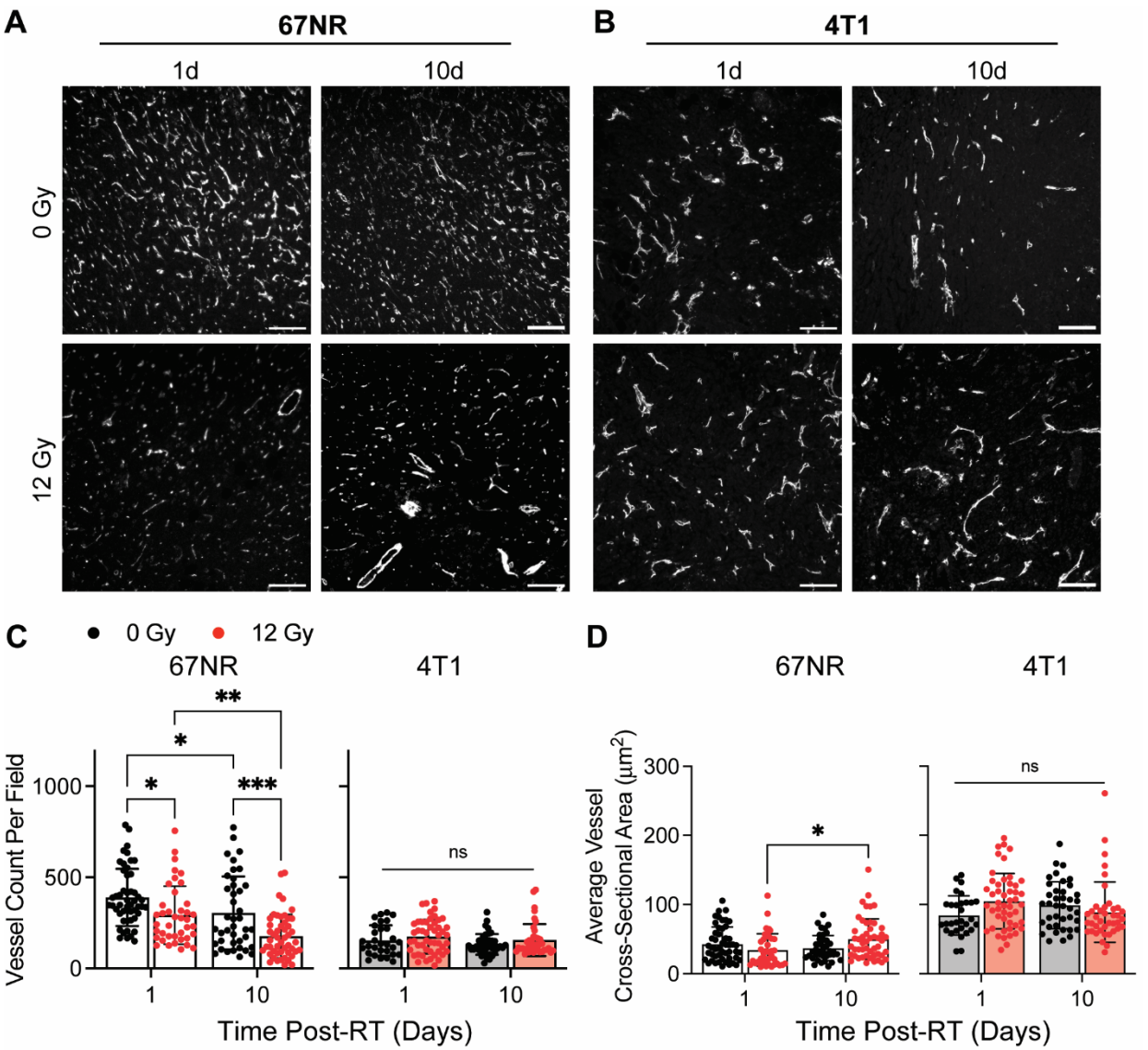

Figure 3. Histology establishes vascular differences after radiation and between tumor types that correspond to US measurements. Representative CD31 immunofluorescence staining of control and irradiated **(A)** 67NR and **(B)** 4T1 tumors at 1 and 10 days post-RT. Scale bar is 100 µm. Quantification of **(C)** the number of $CD31^+$ vessels per field of view (vessel density) and **(D)** the average cross-sectional vessel area per field of view in 67NR (n=5 for 1 day and n=4 for 10 day 0 Gy, n=4 for 1 day and n=5 for 10 day 12 Gy) and 4T1 (n=3 for 1 day and n=4 for 10 day 0 Gy, n=5 for 1 day and n=4 for 10 day 12 Gy) tumors. Error bars represent standard deviation with *p<0.05, **p<0.01, and ***p<0.001 as determined by two-way ANOVA.

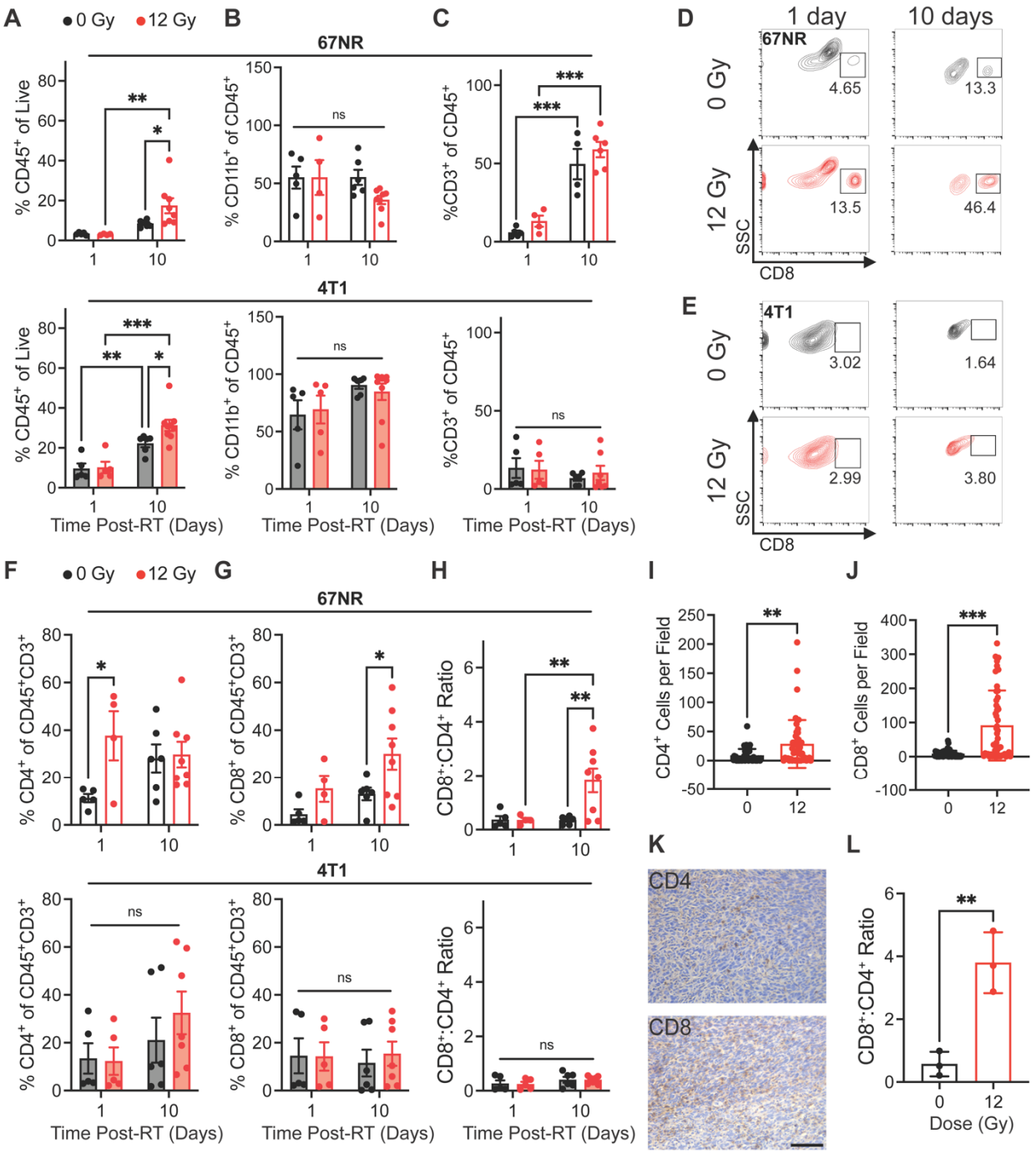

Figure 4. Immune cell infiltration post-RT differs between 67NR and 4T1 tumors. Flow cytometry characterization of tumor-infiltrating immune cell populations at 1 and 10 days post-RT, including general **(A)** $CD45^+$ immune cells, **(B)** $CD11b^+$ myeloid cells, and **(C)** $CD3^+$ T lymphocytes in 67NR (top; n=5 for 1 day and n=4 for 10 day 0 Gy, n=4 for 1 day and n=6 for 10 day 12 Gy) and 4T1 (bottom; n=5 for 1 day and n=6 for 10 day 0 Gy, n=5 for 1 day and n=7 for 10 day 12 Gy) tumors. Representative contour plots showing changes in $CD8^+$ cytotoxic T cells after radiation and over time in **(D)** 67NR and **(E)** 4T1 tumors. Further characterization of T lymphocyte subsets, including **(F)** $CD4^+$ helper T cells, **(G)** $CD8^+$ cytotoxic T cells, and **(H)** the ratio of $CD8^+$:$CD4^+$ T cells in 67NR (top) and 4T1 (bottom) tumors. Ratios calculated from absolute counts of $CD45^+CD3^+CD4^+$ and $CD45^+CD3^+CD8^+$ cells in each tumor. Quantification of

immunohistochemistry staining for **(I)** $CD4^+$ helper and **(J)** $CD8^+$ cytotoxic T cells in 67NR tumors. **K.** Representative images of CD4 and CD8 immunohistochemistry staining in 67NR tumors at 10 days post-RT. Scale bar is 100 µm. **L.** Ratio of $CD8^+$:$CD4^+$ T cells calculated from immunohistochemistry staining of 67NR tumors. Ratios calculated from the average number of cells per field in each condition. n=3 mice per condition. Error bars represent standard deviation with *$p<0.05$, **$p<0.01$, and ***$p<0.001$ as determined by two-way ANOVA.

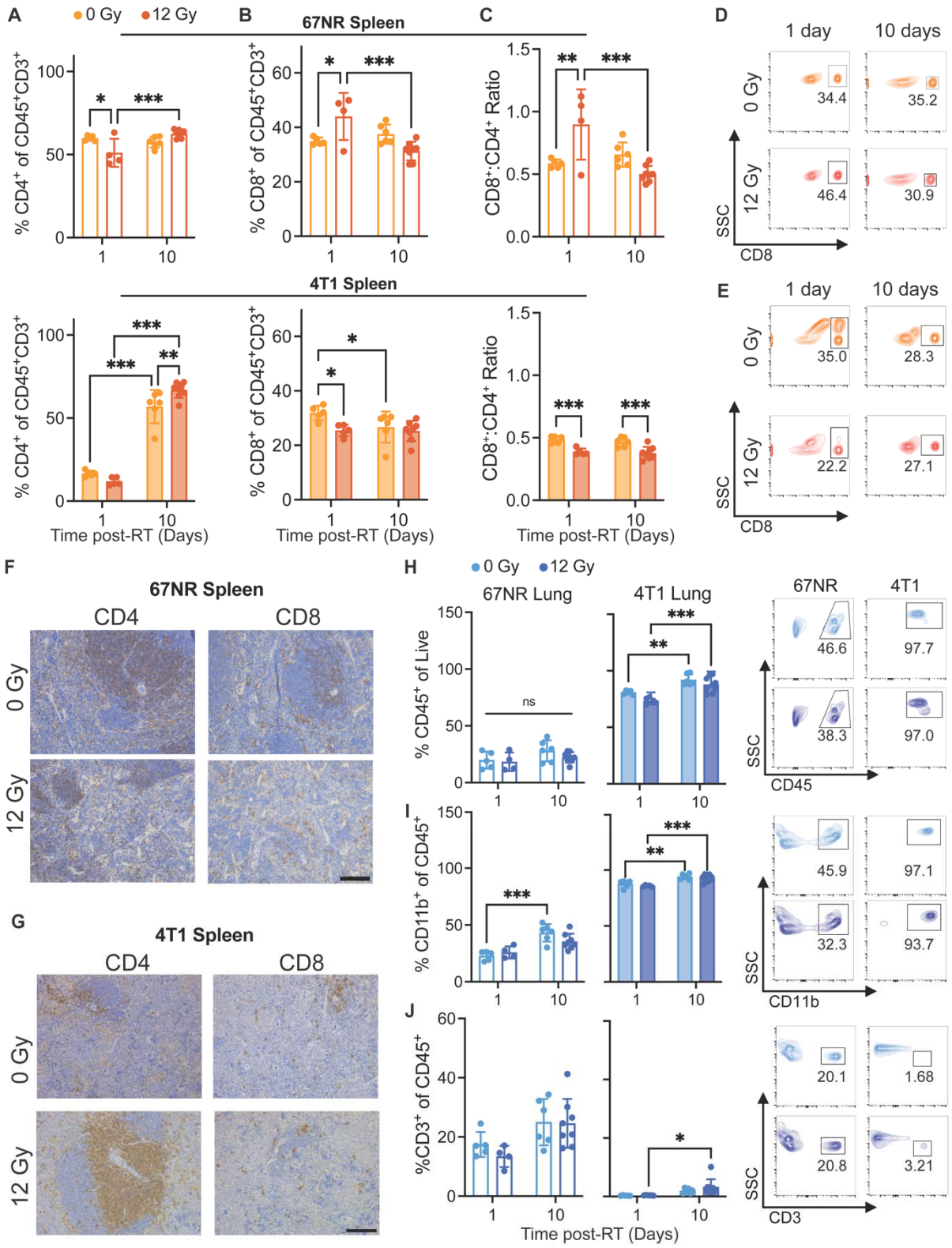

Figure 5. Splenic immune cell changes precede local tumor response to RT in 67NR tumors. Flow cytometry characterization of splenic immune cell populations at 1 and 10 days post-RT, including **(A)** $CD4^+$ helper T cells, **(B)** $CD8^+$ cytotoxic T cells, and **(C)** the ratio of $CD8^+$:$CD4^+$ T cells in spleens from mice with 67NR (top; n=5 for 1 day and n=4 for 10 day 0 Gy,

n=4 for 1 day and n=6 for 10 day 12 Gy) and 4T1 (bottom; n=5 for 1 day and n=6 for 10 day 0 Gy, n=5 for 1 day and n=7 for 10 day 12 Gy) tumors. Ratios calculated from absolute counts of $CD45^+CD3^+CD4^+$ and $CD45^+CD3^+CD8^+$ cells in each spleen. Representative contour plots showing changes in splenic $CD8^+$ T cells after radiation and over time in mice with **(D)** 67NR and **(E)** 4T1 tumors. Representative images of CD4 and CD8 immunohistochemistry staining in the spleens of **(F)** 67NR and **(G)** 4T1-bearing mice at 10 days post-RT. Scale bar is 100 µm. Flow cytometry characterization and representative contour plots of lung immune cell populations at 1 and 10 days post-RT, including **(H)** $CD45^+$ immune cells, **(I)** $CD11b^+$ myeloid cells, and **(J)** $CD3^+$ T cells in lungs of mice with 67NR (left; n=5 for 1 day and 4 for 10 day 0 Gy, n=4 for 1 day and n=6 for 10 day 12 Gy) and 4T1 (right; n=5 for 1 day and n=6 for 10 day 0 Gy, n=5 for 1 day and n=7 for 10 day 12 Gy) tumors. Error bars represent standard deviation with *$p<0.05$, **$p<0.01$, and ***$p<0.001$ as determined by two-way ANOVA.